A Study toward an Improved Understanding of the Relationship between Visible and Shortwave Measurements

ZHANQING LI* AND ALEXANDER TRISHCHENKO

Canada Centre for Remote Sensing, Ottawa, Ontario, Canada

(Manuscript received 2 December 1997, in final form 13 May 1998)

ABSTRACT

Narrowband (NB) to broadband (BB) conversion is a common practice to acquire radiation budget data from operational imagery data. This study attempts to gain further insights into the relationship between NB visible (VIS) albedo and BB shortwave (SW) albedo by means of observational analysis and radiative transfer modeling. Multiple observation datasets were employed including Scanner for Radiation Budget (ScaRaB) satellite measurements, National Centers for Environmental Prediction–National Center for Atmospheric Research reanalysis of precipitable water and temperature profiles, Total Ozone Mapping Spectrometer ozone amount, etc. Radiative transfer modeling was done with an adding–doubling model of high spectral resolution for a range of surface, atmospheric, and cloud conditions. ScaRaB provided calibrated synergistic measurements of VIS and SW albedos. The two types of albedos were found to be linearly correlated with much higher correlation coefficients than previously obtained from other instruments. In combination with other datasets, the impact of various parameters on the VIS–SW relation was investigated and compared with the results of modeling. The most significant parameter influencing the relation is the solar zenith angle, followed by cloud-top height, precipitable water amount, ozone amount, aerosol, and cloud microphysics. Narrow- to broadband conversion models with a varying number of input parameters were developed and validated.

1. Introduction

Albedo at the top of the atmosphere (TOA) is a major variable altering the earth's radiation budget (ERB) and climate. TOA albedo has been monitored by many spaceborne missions such as the Nimbus series (Raschke et al. 1973; Jacobowitz 1984), the ERB Experiment (ERBE) (Barkstrom and Smith 1986), and the Scanner for Radiation Budget (ScaRaB) (Kandel et al. 1994; Kandel et al. 1998). State-of-the-art observation of TOA albedo is made with the Clouds and the Earth's Radiant Energy System (CERES) (Wielicki et al. 1996). Notwithstanding, significant data gaps exist between these research missions. On the other hand, imagery data have been acquired continuously for decades by operational weather satellites such as the National Oceanic and Atmospheric Administration (NOAA) series. Unlike the radiometers measuring ERB, sensors for monitoring clouds are usually not calibrated on board and have narrow spectral coverage in the atmospheric window regions for enhancing contrast between clear and cloudy scenes. To take advantage of the long history of weather satellite observation, surrogate ERB products have been generated from operational satellite observations by means of narrowband (NB) to broadband (BB) conversion (e.g., Gruber et al. 1983).

There are numerous observational and modeling studies concerning the relation between NB and BB albedos. Empirical relations have been derived from an ensemble of NB and BB observations made from different platforms, for example, *Nimbus-7*/Geostationary Operational Environmental Satellite (GOES)-East by Minnis and Harrison (1984), *Nimbus-7*/*NOAA-7* by Wydick et al. (1987), *Nimbus-7*/CZCS (Coastal Zone Color Scanner) by Davis et al. (1984), and *Meteosat-2*/ERBE by Vesperini and Fouquart (1994). Observations made from the same platforms have also been analyzed, for example, *NOAA-9* (ERBE/AVHRR) by Li and Leighton (1992) and Hucek and Jacobowitz (1995). The two latter studies showed much less uncertainty as the NB and BB measurements were made nearly simultaneously. Nevertheless, errors in matching the two types of measurements still hinder the study of NB and BB relations. Note that advanced very high resolution radiometer

* Additional affiliation: Department of Oceanic and Atmospheric Science, Dalhousie University, Halifax, Nova Scotia, Canada.

Corresponding author address: Zhanqing Li, Canada Centre for Remote Sensing, 588 Booth Street, Ottawa, ON K1A 0Y7, Canada. E-mail: Zhanqing.Li@ccrs.NRCan.gc.ca

Unauthenticated | Downloaded 08/11/24 05:42 AM UTC

(AVHRR) and ERBE radiometer had very different fields of view and scanned at different paces. Lack of calibration and differences in the spectral response function (SRF) necessitate derivation of a conversion relation for each NB sensor, even if they are the same types of radiometer. Hucek and Jacobowitz (1995) found that the accuracy of BB albedos estimated from improved-calibration AVHRR NB albedos was even lower than for those estimated from the original AVHRR data using a conversion relation derived by Wydick et al. (1987). This would not be the case, however, if the conversion relation were derived from calibrated data. It is also because of the lack of calibration that Minnis et al. (1995) resorted to a complex multistep conversion approach to estimate BB albedos when no synchronous NB and BB measurements were available. ScaRaB overcomes, to a large extent, the problems of inaccurate match and calibration.

In parallel to the empirical studies, a hierarchy of radiative transfer models (RTMs) has been employed to study the relationship between NB and BB albedos. They span from simple models having a few spectral bands, as used in general circulation models (Cess and Potter 1986), to complex ones having many spectral intervals (Laszlo et al. 1988). The chief merit of modeling lies in that the influence of various factors on the conversion can be readily understood. For example, Cess and Potter found that albedo can be better estimated than radiance or irradiance. Pinker and Laszlo (1988) underlined the importance of accounting for surface spectral and angular dependence. Shine et al. (1984) investigated the effect of including SRF and surface spectral reflectance. Potential accuracy in the estimate of BB albedo over various scene types was assessed by Laszlo et al. (1988). A major limitation of the modeling approach is that models are poorly suited to simulate the complex variations of natural scenes. Nevertheless, they are instrumental in interpreting the observed NB and BB relations.

This study attempts to gain in-depth insights into the NB–BB relation and conversion by means of both observational analysis and radiative transfer modeling. Observations from ScaRaB have many unique advantages to help advance the knowledge of the relation. First, both NB and BB measurements were calibrated on board to allow for direct comparisons with the modeling results. Second, the fields of view (FOVs) of the NB and BB sensors were identical and scanned synchronously so that the two types of measurements can be matched precisely in time and space. Third, ScaRaB flew on a precession orbit, thus providing data with varying solar zenith angle (SZA) for investigating its effects on the conversion. As a result, the NB–BB relations derived from ScaRaB are subject to much fewer uncertainties than those available from any previous missions, allowing for a better understanding of the physics of the conversion.

The paper is structured as follows. The datasets and RTM employed in this study are discussed in the following section. Section 3 addresses the NB–BB relationship and its sensitivities using both observational and modeling data. Development and validation of a set of NB–BB conversions are given in section 4. Section 5 summarizes the study.

2. Datasets and radiative transfer modeling

ScaRaB data are used as the core dataset for studying the NB–BB relation. A combination with other available datasets allows for analyses of the relation's sensitivity to various parameters (such as precipitable water, ozone, and cloud-top height) and the development and validation of NB–BB conversion.

a. TOA NB and BB albedos/fluxes

The ScaRaB is a France–Russia–Germany joint space project. The first ScaRaB radiometer operated from February 1994 through March 1995 onboard the Russian satellite *Meteor-3/7* (Kandel et al. 1998). The FOV of a ScaRaB pixel is about 60×60 km^2 at nadir. Flying on a precession orbit with an inclination angle of 82.5°, ScaRaB provided measurements at all local solar times within a period of approximately seven months. It has four channels: visible (VIS, 0.55–0.65 μm), shortwave (SW, 0.2–4 μm), total (0.2–$>$50 μm), and infrared window (10.5–12.5 μm). This study is only concerned with VIS and SW channels. The normalized spectral response function of the VIS channel is shown in Fig. 1, in comparison with other popular VIS sensors [NOAA/AVHRR, GOES/visible–infrared spin-scan radiometer (VISSR)]. The small discrepancies in the filtering functions of the various sensors can be readily accounted for by modeling. Having done this, the conversion relation derived from ScaRaB can be used for other sensors as well, provided that they are properly calibrated. The visible channel of ScaRaB was calibrated once every two weeks with an onboard lamp. Shortwave calibration was done twice a day with one lamp and twice a month with a second one. Data processing algorithms including scene identification and spectral and angular corrections were adopted from those designed for ERBE (Smith et al. 1986; Viollier et al. 1995). The ERBE SW angular dependence model (ADM) (Suttles et al. 1988) was also employed to convert VIS reflectances to albedos, due to the lack of visible ADM.

The quality of the ScaRaB SW fluxes is comparable to those from the ERBE dataset (Bess et al. 1997), with uncertainties being around 1% for SW components (Kandel et al. 1997; Trishchenko and Li 1998). Eleven months' worth of data were analyzed and were divided into two subsets. The first subset includes March, May, June, August, November, and December 1994 and February 1995; the second contains January 1995 and April, July, and September 1994. The former subset was used in the analysis and development of NB–BB relations,

Unauthenticated | Downloaded 08/11/24 05:42 AM UTC

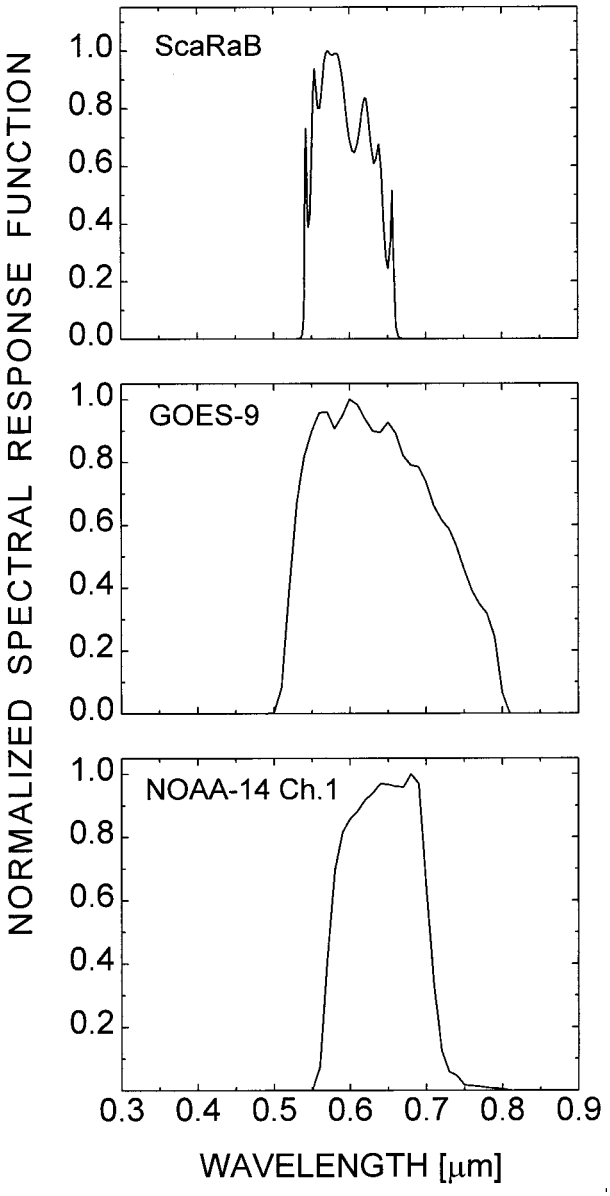

FIG. 1. Normalized spectral response functions of the visible channels of ScaRaB, *GOES-9*/VISSR and *NOAA-14*/AVHRR.

while the latter served as an independent dataset for validation. To avoid the strong correlation between neighboring pixels as revealed by Li and Leighton (1992), the data were highly sampled so that the independence assumption for applying a classical regression technique is not violated. Global ScaRaB data were analyzed separately over ocean, land, snow/ice, desert, and coastal zone, according to geotype information.

b. Precipitable water

Data on precipitable water (PW), or total water vapor content in the atmospheric column, are taken from the reanalysis made by the National Centers for Environmental Prediction (NCEP) and the National Center for Atmospheric Research (NCAR) (Kalnay et al. 1996). The reanalysis was undertaken with a sophisticated state-of-the-art global data assimilation system that incorporates, integrates, and controls the quality of a variety of observational data. While the reanalyzed results for PW data are based primarily on rawinsonde and satellite moisture data, model influence on the reanalysis is apparent for those regions and times lacking observations (Kalnay et al. 1996). In addition to the deficiencies associated with modeling, the reanalysis data for water vapor suffer from limitations inherent in both in situ and remote observations. For example, rawinsonde measurements are only available over a small portion of the earth, mostly near populated areas. Satellite retrievals from Television Infrared Observational Satellite Operational Vertical Sounder are only reliable for clear and thin/partly cloudy scenes, and those from microwave imageries are available over oceans only (Randel et al. 1996). Moreover, the water vapor values as used here were derived from a 12-h analysis, which may contain large sampling errors associated with the diurnal variation of water vapor. Despite the shortcomings, the reanalysis is among the best global uniform datasets currently available. The data are given at 2.5° × 2.5° grids.

c. Cloud-top height

Cloud-top heights were estimated from brightness temperatures derived from ScaRaB IR window channel measurements and the vertical profiles of temperature and geopotential height from the NCEP–NCAR Reanalysis (Kalnay et al. 1996). The profile data were given at the surface, 850, 500, 200, 100, 50, and 20 mb pressure levels at a spatial resolution 2.5° × 2.5°. They were available every 12 h for pressure levels up to 200 mb and once per day at 1200 UTC for 100 mb and above. To account for the atmospheric attenuation in the 10.5–12.5 μm spectral band of ScaRaB (Trishchenko and Khokhlova 1996), brightness temperature (T_{irw}) was corrected as

$$T_{\text{cor}} = -10.85 + 1.053T_{\text{irw}}. \quad (1)$$

The correction ($T_{\text{cor}} - T_{\text{irw}}$) reaches 5 K at $T_{\text{irw}} = 300$ K and diminishes to 0 K at $T_{\text{irw}} = 220$ K. From the corrected temperature and reanalysis profile data, cloud-top height can be determined. Linear interpolation is made between the standard pressure levels. Note that the estimated heights do not represent the geometric tops of the clouds, unless clouds are so thick and uniform within the instrument's field of view that they resemble black bodies. In general, they may be considered as the effective cloud-top heights (H_{eff}) that are somewhere below their geometric heights. For clear scenes as identified by ScaRaB, the cloud-top height is set to zero regardless of temperature.

Unauthenticated | Downloaded 08/11/24 05:42 AM UTC

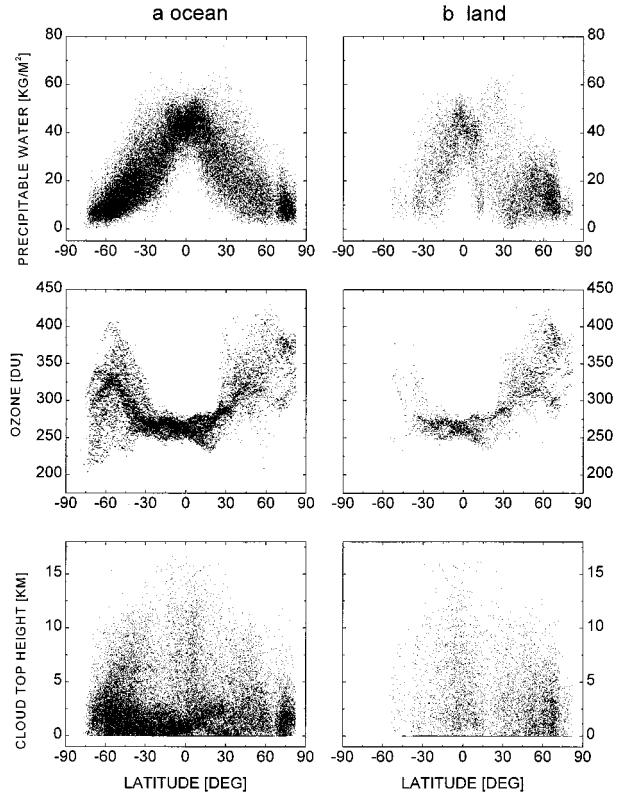

FIG. 2. Variation of precipitable water, ozone, and cloud-top height over (a) global ocean and (b) land with latitude during 1-yr period.

d. Ozone

The vertically integrated ozone amounts employed in this study were retrieved from *Meteor-3*/TOMS (Total Ozone Mapping Spectrometer) measurements. These were made available by the National Aeronautics and Space Administration (NASA)/Goddard Space Flight Center on CD-ROMs. TOMS is a multichannel spectrometer measuring scattered radiation in the ultraviolet range. Based on the difference of reflected radiance between two bands of differential absorption, the total ozone content of the column is inferred (Herman et al. 1996). The absolute and random errors of the inferred ozone amount are both about 3% and are larger at higher latitudes. Daily mean values were used for 1994. The multiyear averages between 1991 and 1994 are substituted for January and February 1995 when no ozone observations were available from TOMS. Gridded daily mean data at a spatial resolution $1.25° \times 1.0°$ are used in this study.

Figures 2a,b show an example of the variability pertaining to PW, cloud-top height, and ozone over ocean (Fig. 2a) and land (Fig. 2b). The nonuniformity of the distributions with respect to latitude is evidently due to the influence of different climatic regimes. The large ranges of variation permit the detection and testing of their effects on the NB–BB relation and the development of conversion models for deriving nonbiased SW albedo. These are the two main objectives of this study.

e. Modeling

Comprehensive radiative transfer modeling is conducted with an adding–doubling RTM (Masuda et al. 1995). The model has 120 unequally spaced special intervals between 0.25 and 22.5 μm, including 41 intervals within 0.3–1 μm, 30 within 1–2 μm, and 34 within 2–5 μm. Hemispheric fluxes in upward and downward directions are computed at 11 streams.

Concurring with the surface-type classification of ERBE, model surface albedos were differentiated according to four basic types: land, ocean, desert, and snow. Grassland is assumed here as a representative of vegetated land whose spectral dependence of albedo is taken from NASA's CERES–Surface and Atmospheric Radiation Budget (SARB) project (Rutan and Charlock 1997). Albedo for vegetated land is characterized by low values in the visible range and a sharp increase at about 0.7 μm. For the grassland studied here, the albedo for visible, near-IR, and broadband ranges is equal to 0.09, 0.3, and 0.19, respectively. A spectrally invariant angular-dependence model was adopted (Dickinson 1983):

$$\alpha(\mu_0) = \alpha_0 \frac{1 + d}{1 + 2d\mu_0}, \tag{2}$$

where α_0 is the albedo for a given spectral interval at SZA $= 60°$, μ_0 is the cosine of SZA, and d is an SZA adjustment factor whose value is 0.22 for grassland. The same angular dependence model is applied to desert and snow but with different values of α_0 (0.36 for desert and 0.86 for snow) and d (0.4 for desert and 0.1 for snow) and different spectral functions, all of which were taken from the CERES–SARB project database. Desert has a higher albedo and less spectral variation than vegetated land. The spectral variation of snow albedo is opposite to that for land. It is high in the visible range and low at longer wavelengths with a much higher broadband albedo. The ocean albedo model is based on Hansen et al.'s (1983) parameterization of Cox and Munk (1956) wave facets theory and Fresnel reflection with the following angular dependence:

$$\begin{aligned}\alpha(\mu_0) = {} & 0.036 + 0.0421(1 - \mu_0)^2 + 0.128(1 - \mu_0)^3 \\ & - 0.04(1 - \mu_0)^4 \\ & + \left(\frac{3.12}{5.68 + \upsilon} + \frac{0.074(1 - \mu)}{1.0 + 3.0\upsilon}\right)(1 - \mu_0)^5,\end{aligned} \tag{3}$$

where υ is wind speed in the lowest atmosphere level ($\upsilon = 10$ m s^{-1} was used). Ocean has the weakest dependence on wavelength.

Corresponding to these surface types are four basic aerosol models: continental, from the World Climate

Unauthenticated | Downloaded 08/11/24 05:42 AM UTC

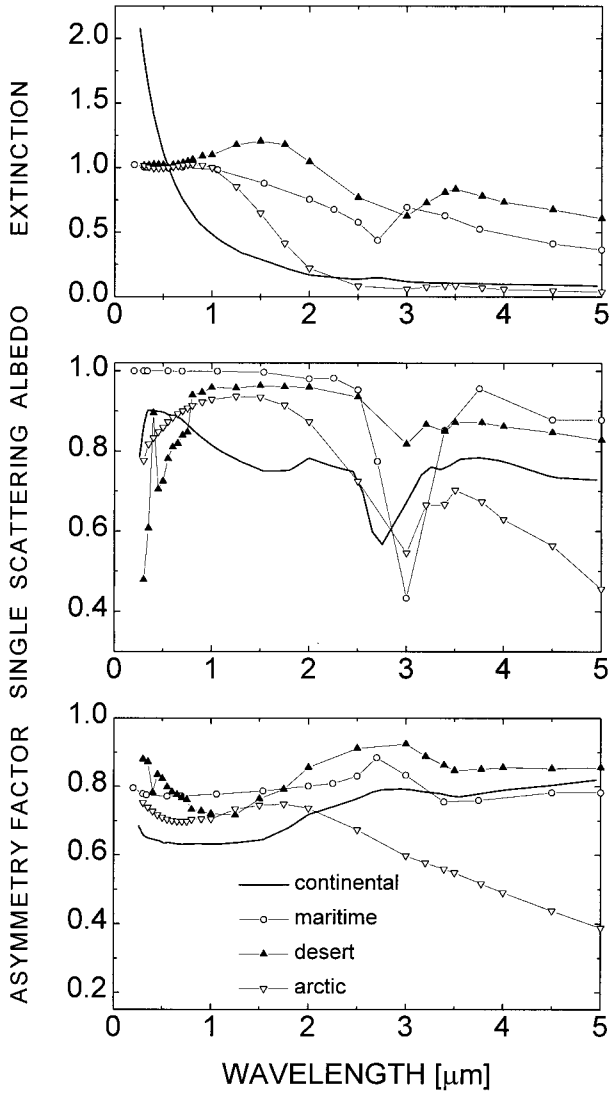

FIG. 3. The spectral functions of normalized extinction coefficient, single scattering albedo, and asymmetry factor for four types of aerosols: continental, maritime, desert, and arctic. The normalization is done with respect to the value at wavelength 0.55 μm. None of the quantities have units.

Program (1986); maritime, from Kneizys et al. (1988); and desert and arctic, both from D'Almeida et al. (1991). Their optical properties are shown in Fig. 3. Aerosol optical thickness ranges from 0 to 1 in the model simulations. Various cloud models of different cloud droplet sizes compiled by Stephens (1979) were used; they were placed at different atmosphere levels above the ground (0–1, 1–2, 2–4, 4–6, and 6–9 km). Cloud optical thickness varies from 0 to 100. The vertical distributions of atmospheric constituents including water vapor and ozone are specified in the tropical, midlatitude–summer, and subarctic–summer model atmospheres (Kneizys et al. 1988). Changes in PW are proportioned to their vertical profiles by scaling the standard profile with altitude-independent factors, except within saturated cloud layers. To simulate ScaRaB measurements, the spectral response function of the ScaRaB VIS channel (cf. Fig. 1) was convoluted with reflected spectral fluxes. This is not needed for the SW BB channel, as the measurements have already been spectrally corrected in ScaRaB data processing.

3. Analysis of the NB–BB relation

The relation between the NB–VIS and BB–SW albedos is seen clearly from the analyses of global ScaRaB measurements for different land cover types and SZAs, as presented in Fig. 4. The relation is linear for all cases. The correlation between visible and SW albedos found here is much higher than previously reported, thanks to the more accurate match between the two types of measurements The linear correlation coefficient reaches almost 1.0 for a small SZA and decreases with increasing SZA. The deterioration of correlation with increasing SZA arises from the magnification of the effects of other factors such as cloud height, water vapor, ozone, and others, as well as from a decrease in the ScaRaB signal-to-noise ratio. The NB–BB relation is different for the four distinct land cover types in terms of slope, intercept, and fit of the linear regression. The linearity of the relation and its dependence on land cover type are consistent with the modeling results (Fig. 5). Each land cover type is tied to a unique aerosol model, for example, continental for land and maritime for ocean. For a given VIS albedo, discrepancies in SW BB albedo due to differences in SZA are over 0.1 for thick clouds.

The modeled and observed relations are similar for all types of surfaces except for snow. The exception is caused by the use of a pure snow model, while natural snow scenes are usually patchy and darker, especially in forests and rugged terrain areas. As cloud thickness increases, there is a tendency for all data points to converge toward the limit of high albedo values. This leads to different slopes and intercepts in the linear relationship. Changes in the slope and intercept with land cover type and SZA are borne out from observations as well. Figure 6 shows the observational values of the slope and intercept. Sizable differences in their magnitudes and trends of variation with SZA are found among the land cover types under examination. These findings suggest that the conversion models should be dependent on scene type and SZA.

In addition to scene type and SZA, sensitivities of the NB–BB relation to other parameters are investigated by analyzing and comparing modeling and observational results. For some parameters, no adequate measurements could be brought to bear. In these cases, only the modeling results are presented. While analyses were done for all types of surface, only the results over ocean and land are shown. To isolate the effect of single parameters, variations in the other parameters were limited

Unauthenticated | Downloaded 08/11/24 05:42 AM UTC

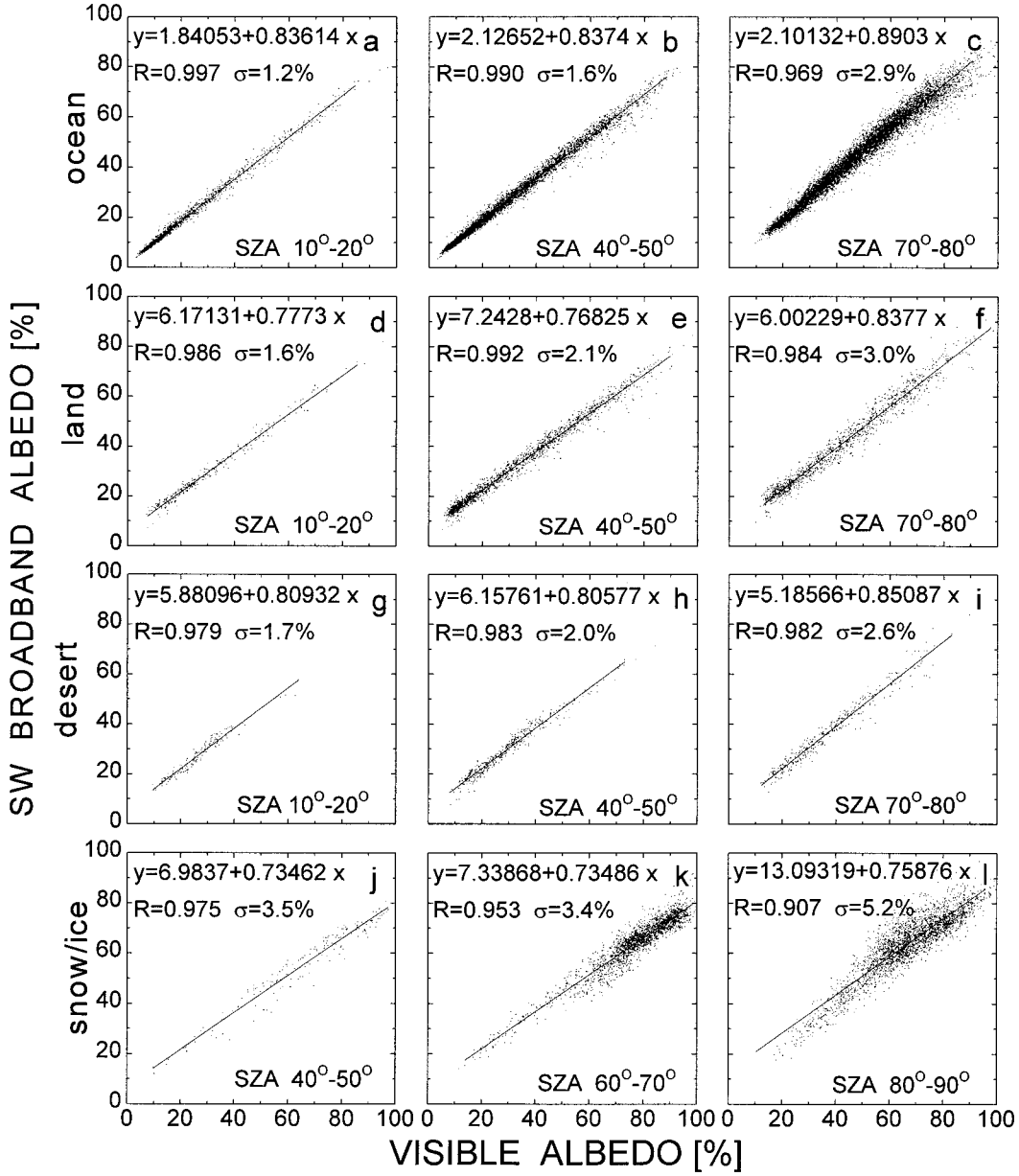

FIG. 4. The relation between VIS and SW albedos with varying SZA over four land cover types: (a–c) ocean, (d–f) land, (g–i) desert, and (j–l) snow/ice, obtained from ScaRaB over the whole globe in 1 yr. The data are sampled sparsely in space and time to eliminate statistical coherence between neighboring pixels.

to small ranges for observational analyses and to fixed values for modeling.

a. Water vapor amount

The effect of PW on the NB–BB relation is discernible from both modeling and observational data. Figure 7 shows the modeled relation between VIS and SW TOA albedos for clear and cloudy oceanic (Figs. 7a,b) and land (Figs. 7c,d) scenes. They are simulated with the cumulus (Cu) cloud model for ocean and stratus (St) cloud model for land with varying optical thickness 0 (clear), 5, 10, 20, 50, and 100. The maritime and continental model aerosols with an optical thickness of 0.1 were used. The VIS and SW albedo observations depicted in Fig. 8 are from ScaRaB observations over oceans (Figs. 8a,b) and land (Figs. 8c,d). Effective cloud-top height H_{eff} is between 0.5 and 1.5 km for ocean and 0.5–2 km for land. Ozone amount was constrained between 250 and 300 Dobson Units (DU). Results for the two SZA intervals of 30°–40° and 70°–80° are shown. They are close to the fixed SZA values used

Unauthenticated | Downloaded 08/11/24 05:42 AM UTC

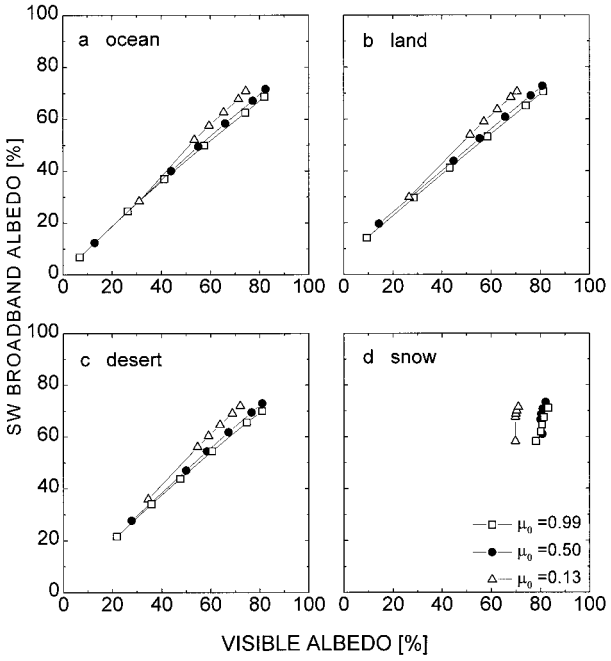

FIG. 5. The modeled VIS–SW relation over four land cover types with different SZA and varying cloud optical thickness. The points along a line from left to right correspond to cloud optical thickness 0 (clear), 5, 10, 20, 50, and 100.

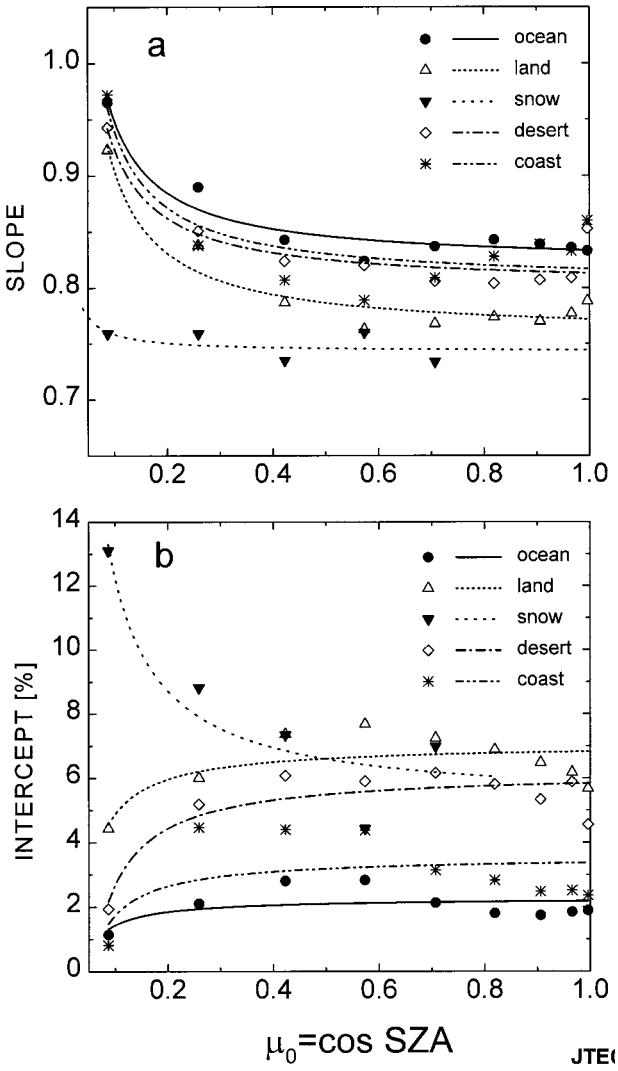

FIG. 6. Variation of the slope and intercept of the VIS–SW relation with SZA derived from ScaRaB over five land cover types. The curves were fit with the function $a + b/\mu_0$.

in modeling (Fig. 7). The scattering of the data points is caused partly by the ranges of the variables and partly by the unbounded changes in other parameters. Despite the scattering, the sensitivity of the relation to PW is similar to that derived from ScaRaB and from the model. The dependence is weak for a small SZA and moderate for a large SZA due to the increase of air mass with SZA. The dependence of the NB–BB relation on PW stems from the difference in responses of VIS and SW albedos to changes in PW. As water vapor increases from 1 to 5 cm, the former remains almost invariant, while the latter decreases moderately (2%–4% for a small SZA and greater than 5% for a large SZA). This is attributed to the spectroscopy of water vapor absorption. Water vapor has strong absorption bands in the near-infrared spectral region but no absorption in the visible band. It should be pointed out that the effect of water vapor depends not only on its total column amount but also on its vertical distribution, especially with respect to the location of a cloud layer. This is seen from the sensitivity of the relation to cloud-top height discussed later.

b. Ozone amount

The influence of ozone on VIS and SW albedos and their relation from modeling and observation are depicted in Figs. 9 and 10, respectively. Model simulations are similar to those used in Fig. 7 except for varying ozone amount and fixed values for other parameters. In view of the observed range of ozone variation delineated in Fig. 2, simulations were done for two ozone amounts: 250 and 375 DU. Likewise, the observational analysis shown in Fig. 10 differentiates ozone amounts into two broad intervals. Variations in PW are limited to 1–2 cm over oceans and 0.5–2 cm over land. For effective cloud-top height, the ranges are 1.5–2.5 km over oceans and 0.5–2 km over land. Broader ranges of parameters for land surface were chosen to increase the number of data points.

In comparison to PW, ozone has a very weak impact of opposite sign on the NB–BB relation, as is seen from both modeling and observational analyses. An increase in ozone amount lowers the VIS albedo but barely alters the SW albedo. Such an effect can be explained by the spectral properties of ozone absorption. Ozone has very strong absorption in the UV band (Hartley band), strong

Unauthenticated | Downloaded 08/11/24 05:42 AM UTC

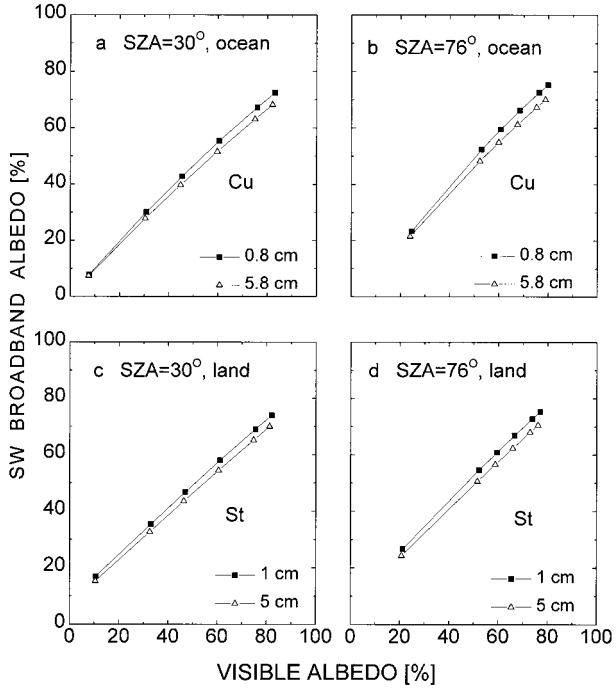

FIG. 7. Sensitivity of the modeled VIS–SW relation to precipitable water over (a), (b) oceans and (c), (d) land with cloud optical thickness varying from 0 (clear) to 100 for two SZAs (30° and 76°). Maritime and continental aerosol models are assumed for ocean and land, respectively, with an optical thickness of 0.1.

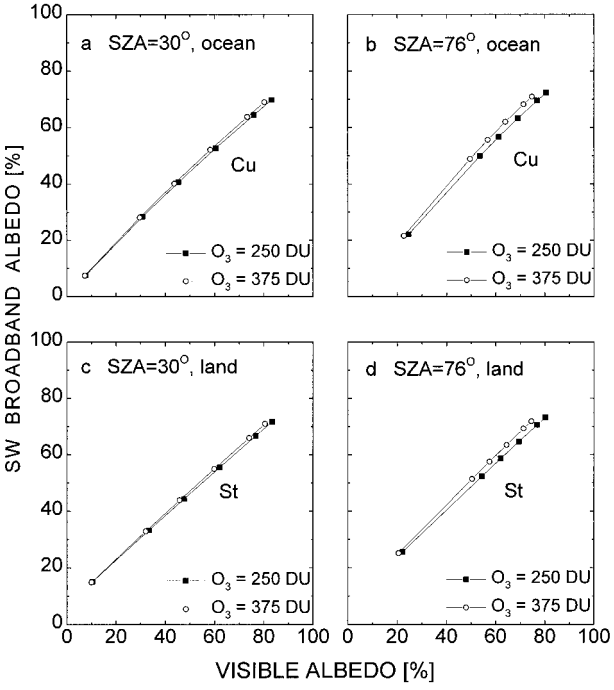

FIG. 9. Sensitivity of the modeled VIS–SW relation to ozone amount over (a), (b) oceans and (c), (d) land for SZAs of 30° and 76°. Cloud optical thickness varies from 5 to 100. Precipitable water is fixed at 5.0 cm over ocean and 3.7 cm over land. Maritime and continental aerosol models are assumed for the two cover types, respectively, with an optical thickness of 0.1.

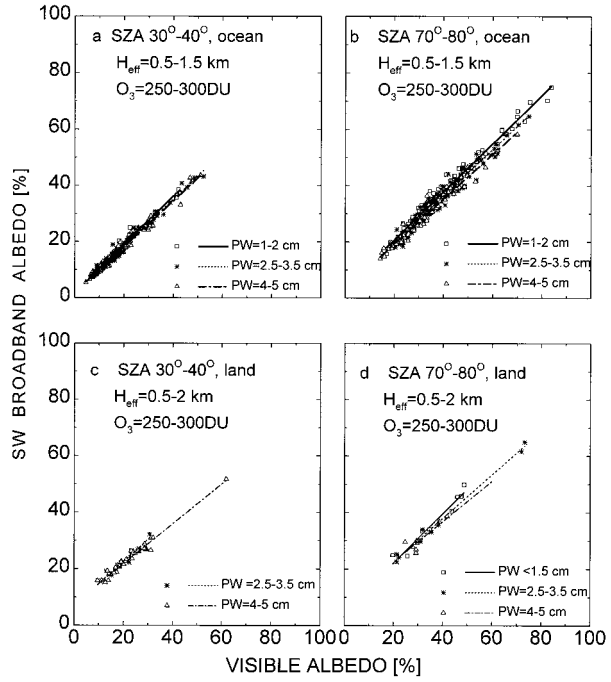

FIG. 8. Sensitivity of the observed VIS–SW relation to water vapor amount obtained from ScaRaB over oceans and land for two different ranges of SZAs. Regressions are derived for three intervals of precipitable water. Variations in other parameters are restricted to the specified intervals.

absorption at the short wavelengths of the visible band (Huggins band), and weak absorption centered around 0.6 μm (Chappius band). The Chappius band affects the relation more than the other two bands that are readily saturated. However, the influence is so small that is hardly detectable from observations for small SZAs due to the low signal-to-noise ratio in the observations. The signal could be enhanced by imposing more rigid constraints on the other parameters, but this would lead to insufficient number of data samples for regression. Similar to PW, ozone also has a more pronounced effect for a larger SZA.

c. Aerosol

With respect to the sensitivity of aerosols, the observational data available for comparison with modeling results is inadequate. Although aerosol optical thickness has been retrieved over oceans (Stowe et al. 1997), it is only available under clear-sky conditions. Since the development of a NB–BB relation requires a range of cloudiness, the analysis is done with modeling data only. Figure 11 shows the sensitivities of the relation to aerosol type and optical thickness. Aerosol particles are situated primarily in the 0–2-km layer with their concentrations decreasing exponentially with height. Two model aerosols of different optical properties are employed.

Unauthenticated | Downloaded 08/11/24 05:42 AM UTC

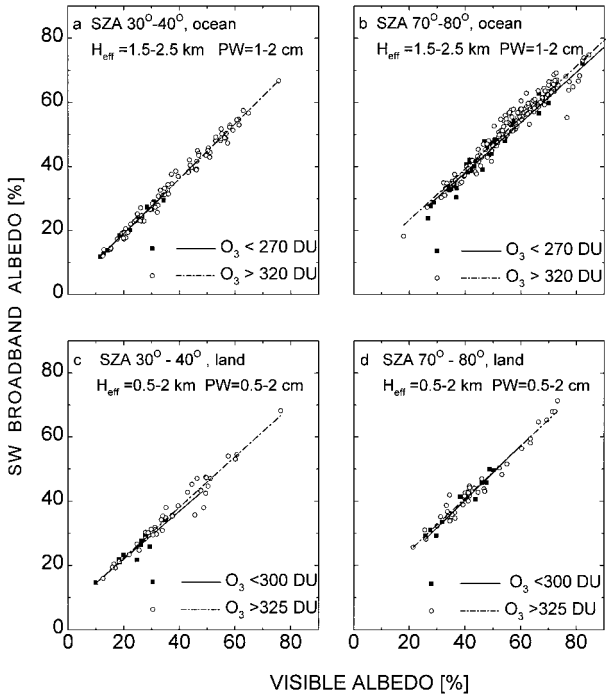

FIG. 10. Sensitivity of the observed VIS–SW relation to ozone amount over oceans and land for two different ranges of SZA. Variations in other parameters are restricted to the specified intervals.

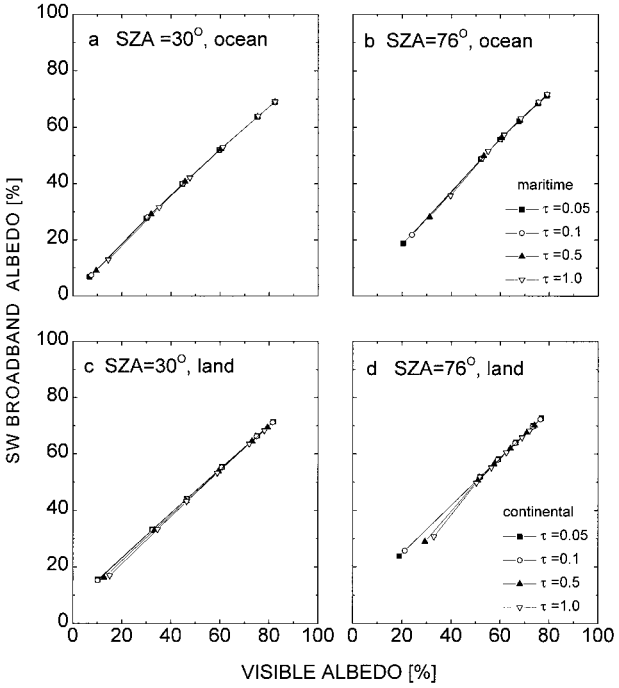

FIG. 11. Sensitivity of the modeled VIS–SW relation to aerosol type and loading. Maritime and continental aerosol models are employed in the simulations, respectively, with optical thickness ranging from 0.05 to 1.0.

The continental aerosol is strongly absorbing, while the maritime aerosol is conservative in scattering. For all simulations, clouds are placed in a 2–4-km atmospheric layer. The maritime aerosol has no impact on the relation since changes in VIS albedo are accompanied by changes in SW albedo in such a manner that the data points lie along the same line. This suggests that the effect of optical properties on the maritime aerosol is analogous to that of clouds as far as the NB–BB relation is concerned. For the continental aerosol, deviations are significant for thin clouds and gradually merged together as cloud optical thickness increases to over 5. In addition to aerosol type, the effect of aerosol depends on surface type. For the same type of aerosol, the response in the NB relation can be quite different when applied to different surface types.

d. Cloud-top height

The influence of cloud-top height on the relation between VIS and SW TOA albedos is imposed in conjunction with other atmospheric parameters. Cloud top separates the atmosphere into two layers that modify the TOA albedo very differently. The lower layer contains the majority of radiatively active media such as water vapor and aerosols. Their impact on TOA albedo is suppressed substantially by the cloud cover aloft. On the other hand, the influence of the atmospheric media situated above the cloud layer such as ozone is reinforced due to the reflection of sunlight by clouds. Besides, the contribution of Rayleigh scattering to the TOA albedo (mainly in the visible band) diminishes as cloud-top height increases due to the reduced effective air mass above the cloud layer. The net effect is that both VIS and SW albedos increase with cloud-top height, as is seen from modeling and observational results shown in Figs. 12 and 13. The slope of the NB–BB relation is very sensitive to cloud-top height. The effect of cloud-top height magnifies, like other parameters, with increasing SZA. For a thick cloud, the estimation of SW albedo according to VIS albedo may introduce an uncertainty larger than 0.15 if the variation in cloud-top height is not considered (cf. Fig. 12).

e. Cloud droplet radius

In principle, cloud microphysics can affect the NB–BB relation through its influence on cloud absorption, which is usually a function of wavelength. For pure cloud droplets, there is negligible absorption in the visible band, whereas absorption in the near-infrared region varies according to cloud microphysics. A weak effect is found from the sensitivity test shown in Fig. 14. The test was done with three typical liquid water cloud models that are differentiated by cloud droplet size distribution only. Their mode radius varies from 3.5 to 7.5 μm. In terms of effective radius it ranges from 6.4 and 13.3 μm, assuming a gamma distribution for cloud drop-

Unauthenticated | Downloaded 08/11/24 05:42 AM UTC

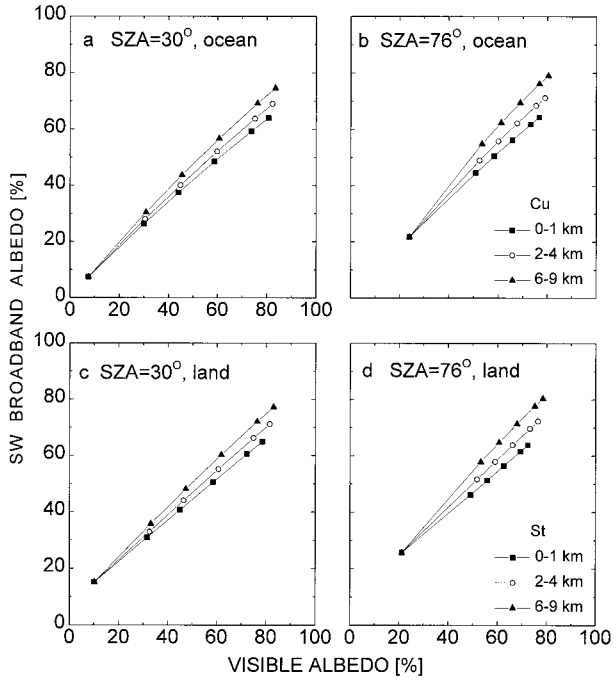

FIG. 12. Sensitivity of the modeled VIS–SW relation to cloud-top height. Cumulus (Cu) and stratus (St) model clouds are placed in different layers.

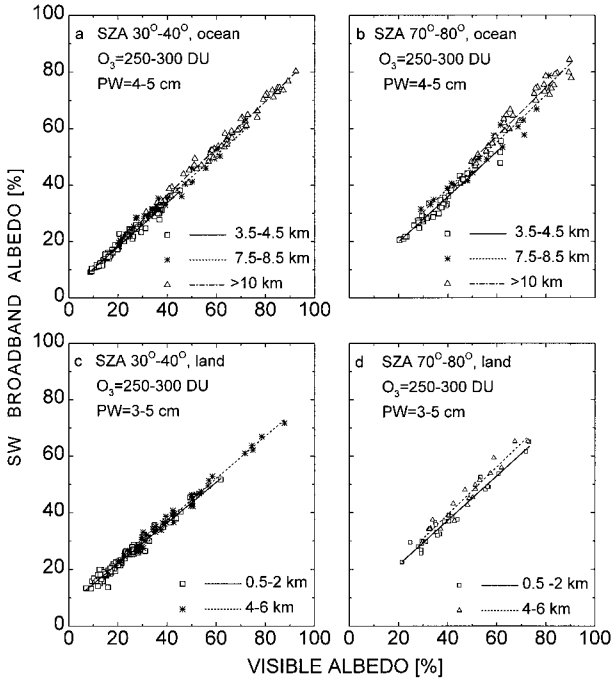

FIG. 13. Sensitivity of the observed VIS–SW relation to cloud-top height. Variations in precipitable water and ozone amount are restricted to the specified intervals. The lines are regressions of the two types of albedos for different ranges of the effective cloud-top height.

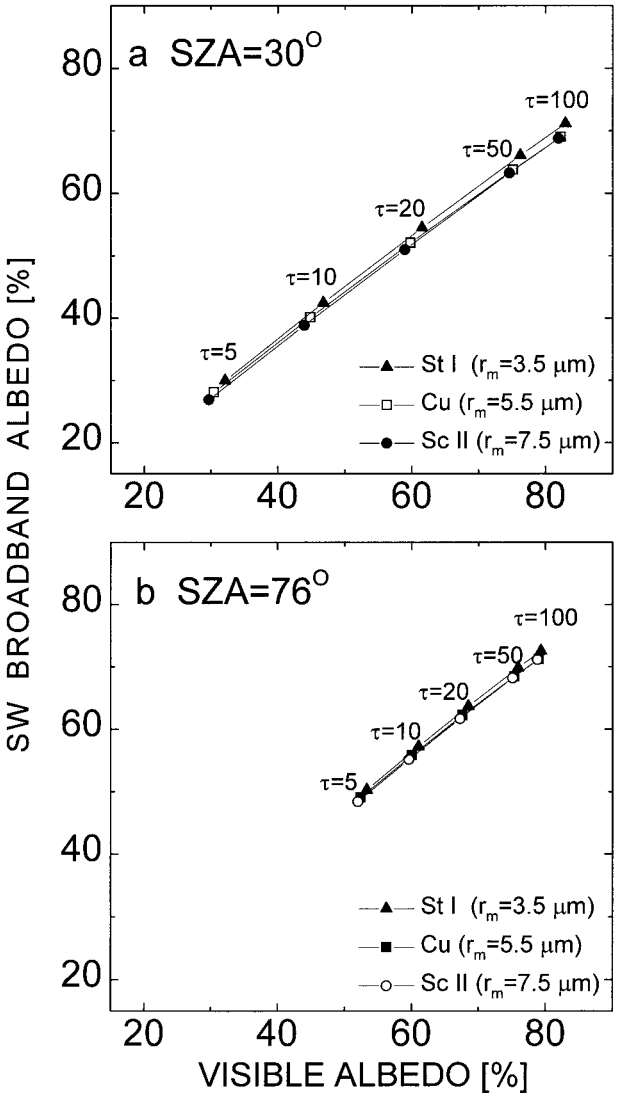

FIG. 14. Sensitivity of the modeled VIS–SW relation to cloud microphysics characterized by different values of mode droplet radius r_m (i.e., the radius corresponding to the maximum droplet concentration) for three model clouds: stratus (St), cumulus (Cu), and stratocumulus (Sc).

let size. It is difficult to detect such a weak dependence with any observational data of cloud microphysics. Unlike the sensitivities to other parameters, the effect of cloud droplet size remains almost invariant throughout the entire range of SZAs.

4. Development and validation of NB to BB conversion models

Three models with different numbers of input parameters were developed by means of conventional regression analysis using data from March, May, June, August, November, and December 1994 and February 1995.

Unauthenticated | Downloaded 08/11/24 05:42 AM UTC

TABLE 1. The regression models of BB albedo (α_{sw}) with a single input variable, visible albedo (α_{vis}).

Surface type	Model	σ_α (%)	σ_F (W m^{-2})	Δ_F (W m^{-2})	N
Ocean	$\alpha_{sw} = 1.736 + 0.878\alpha_{vis}$	2.89	16.3	−3.8	36 474
Land	$\alpha_{sw} = 6.728 + 0.798\alpha_{vis}$	2.76	18.4	−2.9	8558
Snow/ice	$\alpha_{sw} = 10.802 + 0.725\alpha_{vis}$	4.78	20.3	−5.3	7605
Desert	$\alpha_{sw} = 5.266 + 0.839\alpha_{vis}$	2.17	16.8	−1.2	2603
Coastal	$\alpha_{sw} = 3.295 + 0.838\alpha_{vis}$	3.67	22.8	−4.0	2821

The first model is a linear regression between SW albedo (α_{sw}) and VIS albedo (α_{vis}):

$$\alpha_{sw} = a_0 + b_0\alpha_{vis}. \quad (4)$$

Since the model does not require any auxiliary information, it has been most widely used. It is thus referred to as a basic conversion model. The results of regression fitting with this model are given in Table 1. The standard deviation between observed and estimated albedos, denoted by σ_α, ranges from 2.16% for deserts to 4.78% for snow/ice-covered surfaces. In terms of flux (σ_F), it ranges from 16.3 W m^{-2} for oceans to 22.8 W m^{-2} for coastal regions. Due to the variation of incident radiation at the TOA, the application of a regression model derived for estimating albedos gives rise to a systematic error in the flux estimates. For snow/ice scenes the error is as large as −5.3 W m^{-2}. It is interesting to note that the regression coefficients for coastal regions are close to the averages of the coefficients for ocean and land models.

As the most significant parameter modifying the NB–BB relation, SZA is introduced:

$$\alpha_{sw} = a_0 + a_1/\mu_0 + \alpha_{vis}(b_0 + b_1/\mu_0), \quad (5)$$

where $\mu_0 = \cos(\text{SZA})$. This particular form of the function of μ_0 was selected following the findings shown in Fig. 6. More complex functions of μ_0 were also attempted but no significant improvement was achieved. Note that there have been few models containing μ_0 (Minnis et al. 1995; Trishchenko and Li 1998) and their functions are different. The results of fitting with Eq. (5) are presented in Table 2. While the addition of SZA only moderately helps reduce the standard deviations in albedo and flux, it essentially eliminates the overall bias errors in the flux estimates. Reduction in σ_F is substantial for some cover types such as snow. The regression for ocean has a minimum σ_F of 14.0 W m^{-2}. Models for coastal and land regions suffer relatively large random errors with σ_F of 21.8 and 17.2 W m^{-2}, respectively. In terms of σ_α, the largest uncertainty occurs for snow surfaces.

The third model is most comprehensive. It includes all of the parameters under study:

$$\alpha_{sw} = a_0 + a_1/\mu_0 + \sum A_i(a_{2,i} + a_{3,i}/\mu_0) + \alpha_{vis}\left[(b_0 + b_1/\mu_0) + \sum A_i(b_{2,i} + b_{3,i}/\mu_0)\right], \quad (6)$$

where A_i denotes atmospheric parameters (water vapor, ozone, and cloud-top height). While the model is of limited practical utility for operational application, due to the difficulties in obtaining their values, it can be used to demonstrate the potential or upper limit of the estimation uncertainty. The regression models and fitting results are given in Table 3. The improvement is rather small. This is not surprising given the high correlation between NB and BB albedos. The linear correlation coefficients are 0.989, 0.986, 0.983, 0.983, and 0.920 for ocean, land, coastal, desert, and snow, respectively. The remaining small variances can be attributed partially to SZA and atmospheric and surface parameters and partially to model limitations. The input variables convey little information concerning the variation of BB albedo and all measurements contain uncertainties. Moreover, the function of the regression model is not necessarily the most appropriate one.

Data for January 1995 and April, July, and September 1994 were used to further validate the performance of the conversion models. The results of the tests are summarized in Table 4. As in the case of model development, the accuracy of the SW albedo estimates increases somewhat with the number of predictors. For the models with all parameters, global mean bias errors are less than 1 W m^{-2}, while the rms errors are less than 15 W m^{-2}.

Figure 15 plots the latitudinal variations of the differences between observed and estimated SW flux ob-

TABLE 2. The regression models of BB albedo (α_{sw}) with the input variables of VIS albedo (α_{vis}) and cosine of SZA (μ_0).

Surface type	Model	Δ_F (W m^{-2})	σ_α (%)	σ_F (W m^{-2})
Ocean	$\alpha_{sw} = 2.371 - 0.125/\mu_0 + \alpha_{vis}(0.813 + 0.0180/\mu_0)$	−0.55	2.43	14.0
Land	$\alpha_{sw} = 7.637 - 0.357/\mu_0 + \alpha_{vis}(0.741 + 0.0211/\mu_0)$	−0.53	2.46	17.2
Snow/ice	$\alpha_{sw} = 7.047 + 0.166/\mu_0 + \alpha_{vis}(0.704 + 0.0153/\mu_0)$	−0.47	3.86	16.3
Desert	$\alpha_{sw} = 6.578 - 0.492/\mu_0 + \alpha_{vis}(0.787 + 0.0184/\mu_0)$	−0.53	2.10	16.6
Coastal	$\alpha_{sw} = 4.054 - 0.246/\mu_0 + \alpha_{vis}(0.773 + 0.0206/\mu_0)$	−0.42	3.26	21.8

Unauthenticated | Downloaded 08/11/24 05:42 AM UTC

TABLE 3. The regression models of BB albedo (α_{SW}) with the input variables of VIS albedo (α_{vis}), cosine of SZA (μ_0), cloud-top height (H), precipitable water (PW), and ozone content (Z).

Surface type	Model	σ_α (%)	σ_F (W m^{-2})
Ocean	$\alpha_{SW} = 1.987 + 0.0247/\mu_0 + H(0.0959 + 0.0574/\mu_0) - \text{PW}\ (0.00373 + 0.00820/\mu_0) + Z(-0.00164 + 0.00202/\mu_0) + \alpha_{vis}[0.878 - 0.000207/\mu_0 + H(-0.356\text{E-}4 + 0.765\text{E-}3/\mu_0) - \text{PW}\ (0.606\text{E-}3 + 0.254\text{E-}4/\mu_0) + Z(-0.111\text{E-}3 + 0.640\text{E-}7/\mu_0)]$	2.2	13.0
Land	$\alpha_{SW} = 6.913 - 0.0511/\mu_0 + H(-0.421\text{E-}2 + 0.114/\mu_0) + \text{PW}(0.573\text{E-}3 - 0.759\text{E-}4/\mu_0) + Z(-0.740\text{E-}3 + 0.689\text{E-}3/\mu_0) + \alpha_{vis}[0.798 - 0.319\text{E-}3/\mu_0 + H(0.310\text{E-}3 + 0.462\text{E-}3/\mu_0) + \text{PW}(-0.918\text{E-}3\text{-}0.150\text{E-}4/\mu_0) + Z\ (-0.405\text{E-}4 + 0.109\text{E-}5/\mu_0)]$	2.3	16.6
Snow/ice	$\alpha_{SW} = 10.028 - 0.235\text{E-}1/\mu_0 + H(0.523 + 0.495\text{E-}2/\mu_0) + \text{PW}(-0.435\text{E-}1 + 0.157\text{E-}2/\mu_0) + Z(-0.115\text{E-}1 + 0.101\text{E-}4/\mu_0) + \alpha_{vis}[0.725 - 0.136\text{E-}2/\mu_0 + H(0.281\text{E-}3 - 0.527\text{E-}4/\mu_0) + \text{PW}(-0.377\text{E-}3 + 0.109\text{E-}3/\mu_0) + Z(-0.435\text{E-}4 + 0.562\text{E-}4/\mu_0)]$	3.6	15.4
Desert	$\alpha_{SW} = 11.035 - 0.249\text{E-}1/\mu_0 + H(-0.995\text{E-}1 + 0.509\text{E-}1/\mu_0) + \text{PW}(-0.609\text{E-}1 - 0.202\text{E-}2/\mu_0) + Z(-0.166\text{E-}1\text{-}0.417\text{E-}4/\mu_0) + \alpha_{vis}[0.839 + 0.664\text{E-}3/\mu_0 + H(-0.114\text{E-}2 + 0.417\text{E-}3/\mu_0) + \text{PW}(-0.147\text{E-}3 + 0.268\text{E-}4/\mu_0) + Z(-0.113\text{E-}4 + 0.407\text{E-}5/\mu_0)]$	2.0	15.3
Coastal	$\alpha_{SW} = 4.015 + 0.803\text{E-}1/\mu_0 + H(0.520\text{E-}1 + 0.142/\mu_0) + \text{PW}(-0.110\text{E-}2 - 0.786\text{E-}2/\mu_0) + Z(-0.434\text{E-}2 + 0.112\text{E-}2/\mu_0) + \alpha_{vis}[0.838 + 0.970\text{E-}5/\mu_0 + H(0.452\text{E-}3 - 0.885\text{E-}4/\mu_0) + \text{PW}(-0.169\text{E-}3 - 0.665\text{E-}4/\mu_0) + Z(-0.101\text{E-}3 + 0.101\text{E-}4/\mu_0)]$	3.0	20.6

tained by applying the conversion models given in Tables 1–3 to the data for January 1995. The basic model produces differences with a strong zonal variation. The variation is delineated by a curve of the mean differences averaged over 10° latitudinal bins. The global average of zonal absolute mean differences reaches 6.0 W m^{-2}. Other models similar to the basic one lead to even more striking latitudinal variations, as found by Hucek and Jacobowitz (1995). The variation is lessened considerably if the model with SZA is used (Fig. 15b) and almost disappears if the model with all parameters is used (Fig. 15c). The all-parameter conversion model is thus more suitable for evaluating changes in global and zonal mean radiation budget than a simple one.

Note that there are relatively large estimation errors at high latitudes even with the comprehensive model (cf. Fig. 15). The most probable explanation is the misidentification of scene types in these regions. Li and Leighton (1991) found that the ERBE scene identification scheme is prone to large uncertainties over bright snow/ice-covered surfaces. In particular, the scheme tends to misclassify clear, patchy snow/ice areas as partial clouds over snow/ice-free land and ocean (Li and Leighton 1991). Such a misclassification affects the accuracy of albedo estimation. To demonstrate this, comparisons of NB–BB relations for ocean and snow scene types are plotted in Fig. 16. The two sets of data points have little overlap, indicating that different NB to BB conversion models should be employed.

5. Conclusions

Narrowband to broadband conversion is needed to derive the ERB from operational satellite measurements. It is particularly necessary for filling the time gaps between spaceborne ERB missions. While the problem has been addressed in many studies, their results suffer from calibration uncertainties and the lack of coincident NB and BB measurements. These shortcomings were overcome by the use of ScaRaB data that provide calibrated and synergetic NB and BB measurements. As a result, the NB–BB relation derived from ScaRaB is much better defined than that obtained from other sensors. The small uncertainty in the relationship allows for direct comparison between observation and modeling results so that the physics of the conversion can be better understood. To this end, the sensitivities of the NB–BB relation to a variety of parameters were studied by means

TABLE 4. The results of model tests using an independent dataset.

	Global mean difference W m^{-2}				Global rms diffrence W m^{-2}			
Model	Jan	Apr	Jul	Sep	Jan	Apr	Jul	Sep
Basic model	−3.7	2.6	−3.4	−4.9	17.9	12.7	17.5	17.2
Model with SZA	1.2	1.1	−1.4	−0.4	15.8	12.2	15.3	15.8
Model with all parameters	0.6	0.7	−0.3	−0.8	14.8	11.1	14.0	15.1

Unauthenticated | Downloaded 08/11/24 05:42 AM UTC

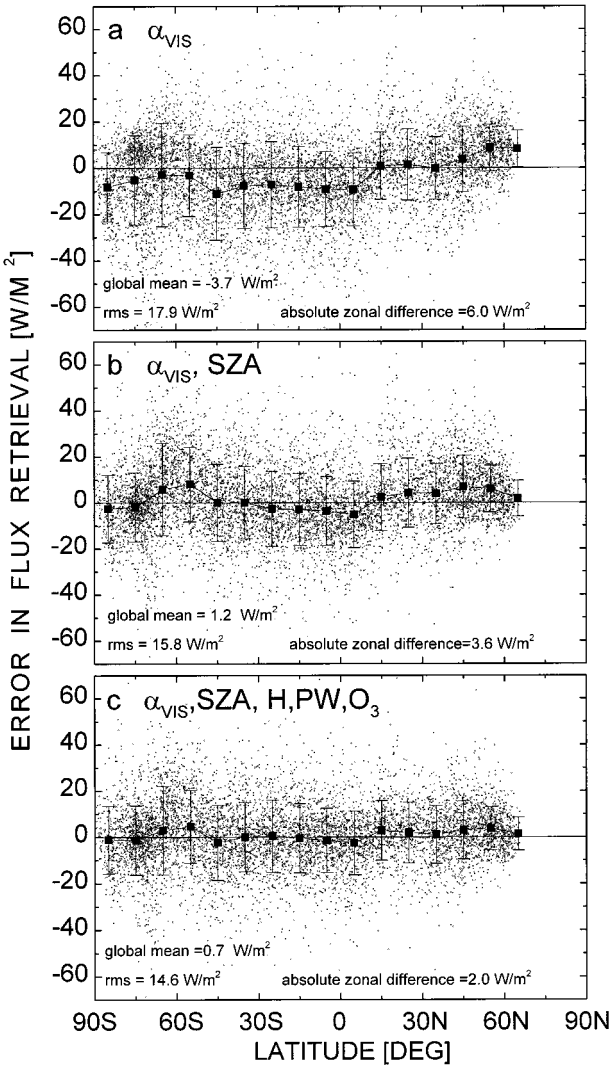

FIG. 15. The differences in SW TOA–reflected fluxes between observation from the ScaRaB BB radiometer and estimation from ScaRaB visible radiometer using NB to BB conversion models. Varying number of input parameters are used: (a) visible albedo only, (b) visible albedo and SZA, and (c) all parameters. Also shown in the plots are global mean differences, global rms differences, and the means of zonal absolute differences for 10° latitude bins. The results are obtained for January 1994.

of radiative transfer modeling and analysis of multiple datasets. Regression models for the conversion were developed and validated. The findings of the study are summarized as follows.

1) The NB and BB albedos are closely correlated in a linear manner. The correlation coefficient is as high as 0.997 for a small SZA and decreases with increasing SZA to 0.907 in the worst case. The deterioration with increasing SZA is due to the enlargement of atmospheric effects and the decrease of the instrument signal-to-noise ratio.
2) The relation between NB and BB albedos is sensitive primarily to surface cover type and SZA; moderately to cloud-top height, PW, and ozone; and weakly to other atmospheric parameters. The results of sensitivity tests are consistent between observation and modeling.
3) Use of visible albedo alone can account for the bulk of variance in SW albedo measurements but leads to bias errors in global and zonal mean fluxes. These systematic errors diminish considerably with the inclusion of SZA as an input variable and almost disappear when other atmospheric parameters are added. However, the random errors remain large for all models. A validation against an independent dataset suggests an overall bias error of less than 1 W m^{-2} and a random error of 11–15 W m^{-2} in reflected flux.

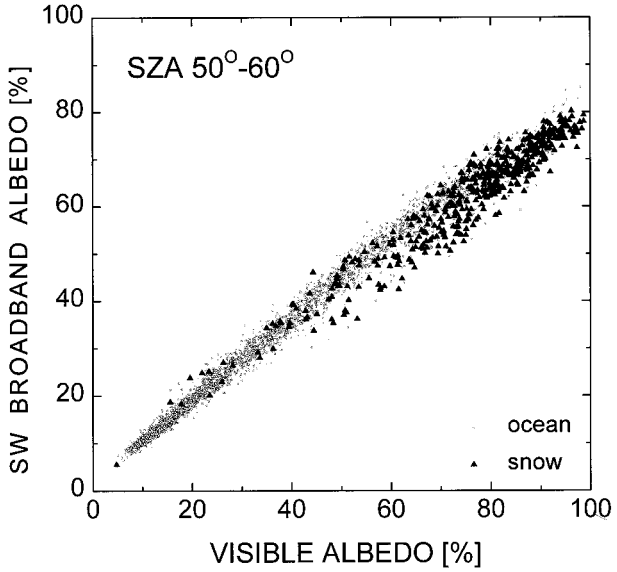

FIG. 16. Comparison of the relation between visible and shortwave albedos over ocean and snow surfaces obtained from ScaRaB.

Acknowledgments. As members of the International ScaRaB Science Working Group, the authors benefit from prompt access to the ScaRaB data with the assistance of ScaRaB staff in CNES and LMD of France. The work is supported in part by the U.S. Department of Energy under Atmospheric Radiation Measurement (ARM) Grant DE-FG02-97ER2361.

REFERENCES

Barkstrom, B. R., and G. L. Smith, 1986: The Earth Radiation Experiment: Science and implementation. *Rev. Geophys.*, **24,** 379–390.

Bess, T. D., G. L. Smith, R. N. Green, D. A. Rutan, R. S. Kandel, P. Raberanto, and M. Viollier, 1997: Intercomparison of scanning radiometer for radiation budget (ScaRaB) and Earth Radiation Budget Experiment (ERBE) results. *Proc. Ninth Conf. on Atmospheric Radiation,* Long Beach, CA, Amer. Meteor. Soc., 203–207.

Cess, R. D., and G. L. Potter, 1986: Narrow- and broadband satellite

Unauthenticated | Downloaded 08/11/24 05:42 AM UTC

measurements of shortwave radiation: Conversion simulations with a general circulation model. *J. Climate Appl. Meteor.,* **25,** 1977–1984.

Cox, C., and W. Munk, 1956: Slopes of the sea surface deduced from photographs of the sun glitter. *Bull. Scripps Inst. Oceanogr.,* **6,** 401–488.

D'Almeida, G. A., P. Koepke, and E. P. Shettle, 1991: *Atmospheric Aerosols: Global Climatology and Radiative Characteristics.* A. Deepak Publishing, 561 pp.

Davis, P. A., E. R. Major, and H. Jacobowitz, 1984: An assessment of *Nimbus-7* ERB shortwave scanner data by correlative analysis with narrowband CZCS data. *J. Geophys. Res.,* **89** (D), 5077–5088.

Dickinson, R. E., 1983: Land surface processes and climate-surface albedos and energy balance. *Advances in Geophysics,* Vol. 25, Academic Press, 305–353.

Gruber, A., I. Ruff, and C. Earnest, 1983: Determination of the planetary radiation budget from TIROS-N satellites. NOAA Tech. Rep. NESDIS 3, U.S. Department of Commerce, Washington, DC, 12 pp. [Available from NOAA, U.S. Department of Commerce, Washington, DC 20233.]

Hansen, J. E., D. Russel, D. Rind, P. Stone, A. Lacis, L. Travis, S. Lebedeff, and R. Ruedy, 1983: Efficient three-dimensional global models for climate studies: Models I and II. *Mon. Wea. Rev.,* **111,** 609–662.

Herman, J. R., and Coauthors, 1996: Meteor-3 Total Ozone Mapping Spectrometer (TOMS) Data Products User's Guide. NASA Ref. Pub., 53 pp. [Available from NASA/Goddard Space Flight Center, Greenbelt, MD 20771.]

Hucek, R., and H. Jacobowitz, 1995: Impact of scene dependence on AVHRR albedo models. *J. Atmos. Oceanic Technol.,* **12,** 697–711.

Jacobowitz, H., and Coauthors, 1984: The Earth Radiation Budget (ERB) Experiment: An overview. *J. Geophys. Res.,* **89,** 5021–5038.

Kalnay, E., and Coauthors, 1996: The NCEP–NCAR 40-year Reanalysis Project. *Bull. Amer. Meteor. Soc.,* **77,** 437–471.

Kandel, R. S., J.-L. Monge, M. Viollier, L. A. Pakhomov, V. I. Adas'ko, R. G. Reitenbach, E. Raschke, and R. Stulhmann, 1994: The ScaRaB project: Earth radiation budget observations from Meteor satellites. *Adv. Space Res.,* **14,** 47–57.

——, and Coauthors, 1998: The ScaRaB earth radiation budget dataset. *Bull. Amer. Meteor. Soc.,* **79,** 765–783.

Kneizys, F. X., E. P. Shettle, L. W. Abreau, J. Chetwynd, G. Anderson, W. Gallery, J. Selby, and S. Clough, 1988: User's guide to LOWTRAN-7, AFGL-TR-88-0177, 140 pp. [Available from AFGL (OPI), Hanscom, AFB, MA 01731-3010.]

Laszlo, I., H. Jacobowitz, and A. Gruber, 1988: The relative merits of narrowband channels for estimating broadband albedos. *J. Atmos. Oceanic Technol.,* **5,** 757–773.

Li, Z., and H. G. Leighton, 1991: Scene identification and its effect on cloud radiative forcing in the Arctic. *J. Geophys. Res.,* **96,** 9175–9188.

——, and ——, 1992: Narrowband to broadband conversion with spatially autocorrelated reflectance measurements. *J. Appl. Meteor.,* **31,** 653–670.

Masuda, K., H. G. Leighton, and Z. Li, 1995: A new parameterization for the determination of solar flux absorbed at the surface from satellite measurements. *J. Climate,* **8,** 1615–1629.

Minnis, P., and E. F. Harrison, 1984: Diurnal variability of regional cloud and clear-sky radiative parameters derived from GOES data. Part III: November 1978 radiation parameters. *J. Climate Appl. Meteorol.,* **23,** 1032–1051.

——, W. L. Smith Jr., D. P. Garber, J. K. Ayers, and D. R. Doelling, 1995: Cloud properties derived from *GOES-7* for spring 1994 ARM Intensive Observing Period using version 1.0.0 of the ARM satellite data analysis program. NASA Ref. Pub. 1366, 58 pp. [Available from NASA/Langley Research Center, 100 NASA Road, Hampton, VA 23681-2199.]

Pinker, R. T., and I. Laszlo, 1988: Comments on ''Narrow- and broadband satellite measurements of shortwave radiation: Conversion simulations with a general circulation model.'' *J. Climate,* **1,** 661–666.

Randel, D. L., T. H. Vonder Haar, M. A. Ringerud, G. L. Stephens, T. J. Greenwald, and C. L. Combs, 1996: A new global water vapor dataset. *Bull. Amer. Meteor. Soc.,* **77,** 1233–1246.

Raschke, E., T. H. Vonder Haar, W. R. Bandeen, and M. Pasternak, 1973: The annual radiation balance of the earth atmosphere system during 1969–70 *Nimbus-3* measurements. *J. Atmos. Sci.,* **30,** 341–364.

Rutan, D., and T. P. Charlock, 1997: Spectral reflectance, directional reflectance, and broadband albedo of the earth's surface. *Proc. Ninth Conf on Atmospheric Radiation,* Long Beach, CA, Amer. Meteor. Soc., 466–470.

Shine, K. P., A. Henderson-Sellers, and A. Slingo, 1984: The influence of the spectral response of satellite sensors on estimates of broadband albedo. *Quart. J. Roy Meteor. Soc.,* **110,** 1170–1179.

Smith, G. L., R. N. Green, E. Raschke, L. M. Avis, J. T. Suttles, B. A. Wielicki, and R. Davies, 1986: Inversion methods for satellite studies of the earth's radiation budget: Development of algorithms for the ERBE mission. *Rev. Geophys.,* **24,** 407–421.

Stephens, G. L., 1979: Optical properties of eight water cloud types. *CSIRO Aust. Div. Atmos. Phys. Tech. Pap.,* **36,** 1–35.

Stowe, L., A. M. Ignatov, and R. S. Singh, 1997: Development, validation and potential enhancement to the second-generation operational aerosol product at the National Environmental Satellite, Data and Information Service of the National Oceanic and Atmospheric Administration. *J. Geophys. Res.,* **102,** 16 923–16 934.

Suttles, J. T., and Coauthors, 1988: Angular radiation models for Earth–atmosphere system. Vol. 1: Shortwave radiation. NASA Ref. Pub. 1184, 114 pp. [Available from NASA/Langley Research Center, 100 Nasa Road, Hampton, VA 23681-2199.]

Trishchenko, A. P., and A. V. Khokhlova, 1996: Using ScaRaB radiometer satellite data for sea-surface temperature determination. *Meteorol. Gidrol.,* **12,** 27–41.

——, and Z. Li, 1998: Use of ScaRaB measurements for validating a GOES-based TOA radiation product. *J. Appl. Meteor.,* **37,** 591–605.

Vesperini, M., and Y. Fouquart, 1994: Determination of broadband shortwave fluxes from Meteosat visible channel by comparison to ERBE. *Beitr. Phys. Atmos.,* **67,** 121–131.

Viollier, M., R. S. Kandel, and P. Raberanto, 1995: Inversion and space–time averaging algorithms for ScaRaB (Scanner for Earth Radiation Budget): Comparison with ERBE. *Ann. Geophys.,* **13,** 959–968.

Wielicki, B. A., B. R. Backstrom, E. F. Harrison, R. B. Lee III, G. L. Smith, and J. E. Cooper, 1996: Clouds and the Earth Radiant Energy System (CERES): An Earth Observing System experiment. *Bull. Amer. Meteor. Soc.,* **77,** 853–868.

World Climate Program, 1986: A preliminary cloudless standard atmosphere for radiation computation. World Climate Program. WCP-12, 53 pp. [Available from the World Meteorological Organization, 41, avenue Giuseppe-Motta, C.P. 2300, Geneva 2, Switzerland.]

Wydick, J. E., P. A. Davis, and A. Gruber, 1987: Estimation of broadband planetary albedo from operational narrowband satellite measurements. NOAA TR-NEDIS 27 to the U.S. Department of Commerce, Washington, DC, 32 pp. [Available from NOAA, U.S. Department of Commerce, Washington, DC 20233.]

Unauthenticated | Downloaded 08/11/24 05:42 AM UTC